Improved state of charge estimation for Li-ion batteries using fractional order extended Kalman filter

Kodjo S.R. Mawonou, Akram Eddahech, Dominique Beauvois, Emmanuel Godoy, Didier Dumur

Improved state of charge estimation for Li-ion batteries using fractional order extended Kalman filter

Kodjo S. R. MAWONOU[a,b,*], Akram EDDAHECH[b], Didier DUMUR[a], Dominique BEAUVOIS[a], Emmanuel GODOY[a]

[a] *Laboratoire des Signaux et Systèmes (L2S, UMR 8506), CentraleSupélec - CNRS - Université Paris-Sud, Université Paris-Saclay. 3, Rue Joliot Curie, 91192, Gif-sur-Yvette, France.*
[b] *Technocentre Renault, 1 Avenue du Golf, 78280 Guyancourt, France.*

Abstract

An accurate state of charge (SoC) estimation by the battery management system (BMS) is crucial for efficient and non-destructive battery operation in automotive applications. The model identification of these batteries has consistently been the critical point to meet good accuracy. To that extent, a fractional order model (FOM) is derived, which provides a more meaningful insight into the battery physical phenomena without increasing the number of parameters as opposed to electrochemical models. This paper proposes FOM identification for Li-ion batteries in both frequency domain based on recorded impedance spectroscopy (EIS) data and time domain using a recursive least squares (RLS) algorithm. Fractional derivatives are overly sensitive to the value of their fractional order. A straightforward and efficient way to identify the fractional orders based on recorded EIS data is proposed in this paper. Furthermore, an extended Kalman filter (EKF) is also designed based on the derived model to estimate the SoC. The designed fractionasl order filter provides a higher accuracy level in comparison to the classical equivalent electric circuit (EEC). Various results at several temperatures and driving profiles for both PHEV and EV batteries confirm that the FOM provides better accuracy and robustness compared to the classical integer order model.

Keywords: Li-ion battery; Fractional order model; Electrochemical impedance spectroscopy; EKF; SoC estimation; Recursive identification.

1. Introduction

Electrified vehicles (EV, PHEV and HEV) are promising technologies to overcome CO2 emission issues. These green vehicles rely on a core component which is the battery. In order to make these electrified vehicles widespread in the global market, car users need to be comforted in terms of security and benefit such as autonomy and rechargeability.

Despite of Lithium-ion (Li-ion) cells are the most commonly used, due to their high energy, power densities and their longer lifespan[1], recently, deep researches are animated on battery technologies to ameliorate their global cells electrochemical performances compared to today NMC lithium-ion like recent studies on solid-state battery [2, 3, 4].

*Corresponding author
Email address: kodjo.mawonou@centralesupelec.fr (Kodjo S. R. MAWONOU)

The fact that battery packs are made of numerous electrochemical cells makes the control of such complex system mandatory. The battery management system BMS [5] represents a key point to ensure exploring these new emerging technologies with optimized functional and safety aspects. The BMS is dedicated to ensuring not only diagnosis (fault detection from communication for example) and battery safety (prevent overvoltage, undervoltage, overcurrent and overtemperature) but also handle battery state estimators and balancing. This paper precisely considers chemistry algorithms part in the BMS software. Predominantly battery model improvement and SoC estimation are discussed.

Efficient and cautious use of Li-ion batteries typically requires the monitoring of numerous variables like the state of charge (SoC), the state of health (SoH), the acceptable/available power when charging/discharging, the charge capacity and the internal resistance [6, 7, 8]. Unfortunately, these variables are not directly measurable. The BMS has to estimate each of them, thanks to measured data such as current, voltages, temperatures and state observers [9]. Besides, these parameters change over time and charge-discharge cycles. These changes have to be taken into account to ensure a maximal level of performance, throughout the life of the battery [10]. The lifetime of the battery is maximized by facilitating an ideal operating condition [11, 12].

The accuracy of estimations provided by the BMS depends on the chosen battery model. Given that batteries have complex electrochemical mechanisms and highly non-linear behaviour, it is challenging to accurately design easily implementable models. Several models are considered in the literature, such as equivalent electric circuit (EEC), electrochemical model (EM), fractional order model (FOM) and neural network models (NN). EEC models are made of a few resistor-capacitor (RC) networks in series with a voltage source corresponding to the open circuit voltage (OCV) of the battery. These models are the most commonly used and are easy to operate, but they produce an insufficient level of accuracy. A detailed framework of EEC models for Li-ion batteries SoC estimation is given in [13, 9, 14]. Electrochemical models, however, are based on a set of partial differential equations (PDEs) that describe the electrochemical reactions that take place inside the battery [15]. Several parameters are to be identified involving sometimes destructive tests for the battery. In addition, the uncertainty from parameter identification makes these models hard to operate. These models are frequently utilized for design purposes and are unsuitable for on-line applications. There were several attempts to simplify these models leading to single particle models (SP) [16, 17]. Nevertheless to the best of our knowledge, there is no electrochemical operated BMS. Black box approaches such as neural network models [18, 19] or adaptive neuro-fuzzy inference system (ANFIS) [20] produce satisfying results if enough training data are available. On several occasions this approach lacks robustness and demands high computational resources.

Latterly, it has been reasoned that solving SP models leads to fractional order equations [21, 22]. Also, the impedance frequency response of a Li-ion battery displays at low frequencies behaviours that are easily captured by constant phase or Warburg elements (CPE). The use of CPEs leads to fractional order model. Moreover, FOM may improve SoC estimation accuracy while involving fewer parameters than the classical n-RC equivalent circuit models. This observation has led to a growing number of attempts to build FOM for Li-ion battery monitoring [23, 24, 25]. In [24] a continuous time state-variable filter was used to estimate parameters for a Li-ion battery. The author argued

that using instrumental variable helped to improve the accuracy of the output of the least square algorithm used. The fractional order in his study was achieved by fitting the output voltage of his identified model to the measured voltage of the battery. In [26] a multi-swarm cooperative particle swarm optimization (MCPSO) is used to identify fractional order parameters for a Li-ion battery based on federal city driving schedule experimental data. In [27] a FOM was designed based on frequency domain identification using particle swarm optimization (PSO). A hybrid multi-swarm particle swarm optimization (HMPSO) was used in [25] to identify a FOM based on training data of eight Li-ion cells. All these approaches are based on classical optimization used on time domain or frequency domain data. Fractional derivatives are overly sensitive to the value of their fractional order. Therefore, time domain identification is extremely sensitive to the initialization and noise level. The frequency domain approaches in the literature do not take advantage of the structure of the studied model. This paper presents a swift, straightforward and efficient way to identify the fractional orders based on recorded EIS data for Li-ion batteries.

The present paper aims to propose a complete framework for a high fidelity EKF SoC estimator based on identified fractional order model parameters in the frequency domain for Li-ion batteries. The remainder of this paper is organized as follows. The following section describes fractional order derivatives. Section 3 displays FOM models for Li-ion batteries with a presentation of a new frequency domain identification procedure, a time domain identification and their numerical approximation. A fractional order EKF based on the identified model is designed and discussed in Section 4. Ultimately, conclusions are presented in Section 5.

2. Fractional derivatives

Fractional-order calculus (FOC) is an extension of the classic integer-order derivative. The idea of fractional calculus emerged in the development of integer-order calculus. The first literature reference is associated with a letter, from Leibniz to l'Hospital in 1695 [28]. FOC are broadly used at present for diverse topics such as diffusive systems, electrical systems, control, etc [29]. Several fractional derivatives and integrals exist [30], but the most commonly used fractional derivatives in the literature are: the Riemann-Liouville (RL) definition, the Caputo (CP) definition, and the Grünwald - Letnikov (GL) definition.

RL derivation of a causal function f of time t at order $\alpha \in \mathbb{R}_+^*$ definition is given as [31, 28]:

$$\mathcal{D}_{RL}^{\alpha} f(t) = \frac{1}{\Gamma(n-\alpha)} \frac{d^n}{dt^n} \int_0^t \frac{f(\tau)}{(t-\tau)^{\alpha-n+1}} \mathrm{d}\tau \tag{1}$$

where $n-1 < \alpha < n$, $n \in \mathbb{N}$ and $\Gamma(.)$ is *Euler's Gamma* function defined in Eq. 2.

$$\Gamma(n) = \int_0^t t^{n-1} e^{-t} \mathrm{d}t \tag{2}$$

CP derivation of a causal function f of time t at order $\alpha \in \mathbb{R}_+^*$ definition is given as:

$$\mathcal{D}_{CP}^{\alpha} f(t) = \frac{1}{\Gamma(n-\alpha)} \int_0^t \frac{f^{(n)}(\tau)}{(t-\tau)^{\alpha-n+1}} \mathrm{d}\tau \tag{3}$$

where $n-1 < \alpha < n$, $n \in \mathbb{N}$, $\Gamma(.)$ is the *Gamma* function and $f^{(n)}$ is the n-th integer order derivative of the temporal function f.

GL derivation of a causal function f of time t at order $\alpha \in \mathbb{R}_+^*$ definition is given as:

$$\mathcal{D}_{GL}^{\alpha} f(t) = \lim_{T_s \to 0} \frac{1}{T_s^{\alpha}} \sum_{j=0}^{\lfloor t/T_s \rfloor} (-1)^j C_{\alpha}^j f(t - jT_s) \tag{4}$$

where T_s is the sampling time and $\lfloor t/T_s \rfloor$ the integer part of t/T_s, C_{α}^j the Newton binomial coefficient generalized to real numbers using Eq. 5.

$$C_{\alpha}^j = \frac{\Gamma(\alpha+1)}{\Gamma(j+1)\Gamma(\alpha-j+1)} = \frac{\alpha(\alpha-1)\dots(\alpha-n+1)}{n!} \tag{5}$$

GL fractional derivative is the most used definition for numerical applications in the literature.

Frequency domain representation of a Fractional order transfer (FOT) function can be written as follows [32, 33]:

$$H_z(s) = \frac{b_M s^{\nu_{b_M}} + b_{M-1} s^{\nu_{b_{M-1}}} + \ldots + b_0 s^{\nu_{b_0}}}{a_N s^{\nu_{a_N}} + a_{N-1} s^{\nu_{a_{N-1}}} + \ldots + a_0 s^{\nu_{a_0}}} \tag{6}$$

where $s \in \mathbb{C}$ is the Laplace variable. One can then derive a fractional-order differential equation of the form [32, 33]:

$$a_N \mathcal{D}^{\nu_{a_N}} y(t) + a_{N-1} \mathcal{D}^{\nu_{a_{N-1}}} y(t) + \ldots + a_0 \mathcal{D}^{\nu_{a_0}} y(t) = b_M \mathcal{D}^{\nu_{b_M}} u(t) + b_{M-1} \mathcal{D}^{\nu_{b_{M-1}}} u(t) + \ldots + b_0 \mathcal{D}^{\nu_{b_0}} u(t) \tag{7}$$

where $\mathcal{D}^{\nu}$ denotes the RL, CP or GL fractional derivative depending on initial conditions and their physical meaning, and $a_0 = 1$ conventionally. A state-space representation of a fractional-order linear time-invariant system is given as follows:

$$\begin{cases} \mathcal{D}^{\alpha} x(t) &= Ax(t) + Bu(t) \\ y(t) &= Cx(t) + Du(t) \end{cases} \tag{8}$$

where $x \in \mathbb{R}^n$ is the state vector, $u \in \mathbb{R}^m$ the input variable, and $y \in \mathbb{R}^p$ is the output vector of the system; $A \in \mathbb{R}^{n \times n}$, $B \in \mathbb{R}^{n \times m}$, $C \in \mathbb{R}^{p \times n}$, $D \in \mathbb{R}^{p \times m}$, and $\alpha = [\alpha_1,\ \alpha_2,\ \ldots \alpha_n]^T$ are the fractional orders. If $\alpha_1 = \alpha_2 = \ldots = \alpha_n \equiv \alpha$, the system in Eq. 8 is of commensurate-order, otherwise it is of an incommensurate-order [33, 28, 31]. For fractional order system stability, one can refer to theories developed in [34, 29] for commensurate-order systems.

3. Fractional-order model for Li-ion batteries

The state of systems with diffusion at a given time depends on their configuration at previous times. Fractional-order derivatives take into account this history in its definition as a convolution with a function of which the amplitude decays at earlier times as a power-law of time [28]. Fractional-order transfer functions (FOTs) allow the use of a more compact representation of a system where the classical integer transfer would demand a high order model [33]. There is an extensive literature of FOM used for Li-ion batteries modeling. Two alternative approaches exist to justify the use of fractional-order elements.

To begin with, one can use the frequency domain representation of the impedance of the battery, based on impedance spectroscopy data, and derive a transfer function of its internal impedance [35, 36, 37]. The use of constant phase elements to model the frequency domain behaviour of Li-ion batteries leads to FOMs, given that CPEs are defined using Eq. 9:

$$CPE(j\omega) = \frac{1}{C\omega^{\alpha}\left[\cos\left(\frac{\alpha\pi}{2}\right) + j\sin\left(\frac{\alpha\pi}{2}\right)\right]} \tag{9}$$

where $\alpha \in [0, 1]$ is the fractional exponent and the constant-phase value is $-\frac{\alpha\pi}{2}$. In [38] CPEs were used in combination with a recurrent neural network (RNN) to monitor the behaviour and state of health (SoH) of Li-ion batteries. In [39] a FOM sliding mode observer for SoC estimation based on frequency domain identification was designed.

Next, one can equally utilize simplified electrochemical models as for instance in [21, 22, 40] where single particle models (SPMs) were used to design fractional-order transfer functions.This approach is more accurate than the previous one but requires identification of many parameters that may be destructive for the batteries. In this paper, the first approach was adopted leading to a second order FOM circuit displayed in Fig. 1.1. This is associated with the use of two CPEs to reproduce the frequency domain behaviour of the battery. The first CPE represents the charge transfer phenomenon at the electrodes whereas the second represents lithium diffusion.

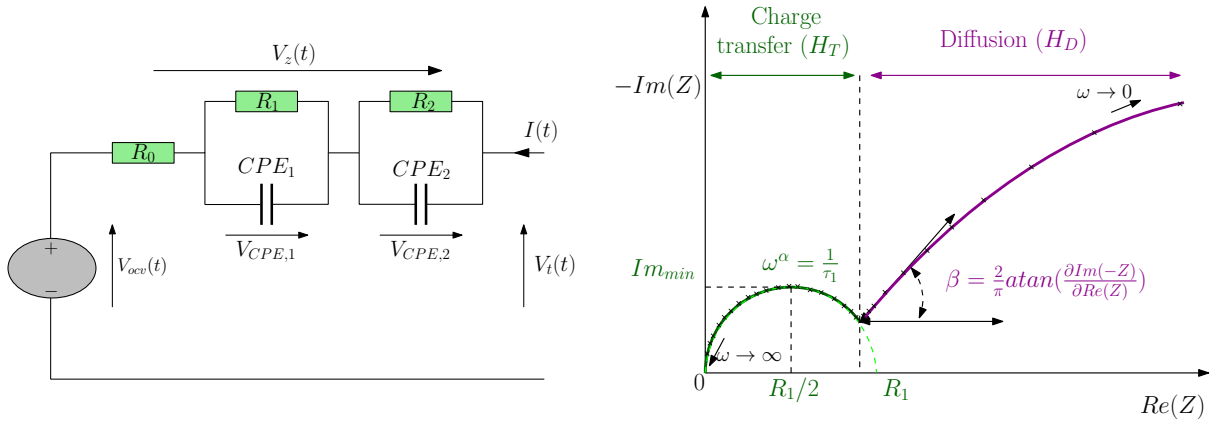

(1.1) 2^{nd} order equivalent circuit using two CPEs. V_t is the measured terminal voltage and I is the measured input current.

(1.2) Frequency domain representation of H_z illustration.

Figure 1: 2^{nd} order fractional model representation of a Li-ion battery.

The transfer function corresponding to the displayed circuit in Fig. 1.1 is given by Eq. 10:

$$H_z(s) = R_0 + \frac{R_1}{1 + \tau_1 s^{\alpha}} + \frac{R_2}{1 + \tau_2 s^{\beta}} \tag{10}$$

To identify the parameters of this model, both frequency and time domain identifications was conducted. The frequency domain identification results based on recorded EIS data at various SoCs are used as initial guess for the time domain identification to achieve rapid convergence.

3.1. *Frequency domain identification*

The frequency domain identification is conducted using recorded EIS data. The measurement was carried out in a galvanostatic mode using a Bio-Logic VMP300 with a 20 A booster and EC-Lab® software package. The EIS data were collected within the frequency range of 10 mHz to 10 kHz using 10 frequency points per decade. The amplitude of the applied current was 1 A (RMS), approximatively $C/100$ for EV cells and of course adapted for PHEV cells as well. The cells were introduced in a climatic chamber and well thermalized. The measured temperature is around $+/-2\ ^{\circ}C$ of the target one.

There are frequency domain FOM identification tools in the literature such as: CRONE toolbox [41], or FOMCON toolbox [42] based on Hartley [43], Levy's or Vinagre [44] algorithms for commensurate FOT. This paper takes advantage of the structure the studied model to propose a novel approach to identify its parameters without using any of the existing algorithms. One can model the frequency domain response of the transfer function H_z using the representation in Fig 1.2.

The ohmic resistance R_0 is easily retrieved, as one can set its value to the real part of the transfer function H_z when its imaginary part is equal to zero. The impedance of the charge transfer part is described using Eq. 11:

$$H_T(s) = \frac{R_1}{1+\tau_1 s^{\alpha}} = \frac{R_1}{1+\tau_1\omega^{\alpha}\cos\left(\frac{\alpha\pi}{2}\right)+j\tau_1\omega^{\alpha}\sin\left(\frac{\alpha\pi}{2}\right)} \tag{11}$$

When $Im\left(H_T(j\omega)\right)$ reaches its maximum value, one can compute the charge transfer resistance R_1 and the charge transfer time constant τ_1 using Eq. 12:

$$\tau_1 = \left(\frac{1}{\omega_{min}}\right)^{\alpha} \tag{12a}$$

$$R_1 = 2Re\left(H_T(j\omega)\right) \tag{12b}$$

where ω_{min} is the corresponding measurement frequency. Noting the imaginary part for that frequency $Im_{min} = -Im(H_T)$ one can compute its fractional exponent using Eq. 13:

$$\alpha = \frac{2}{\pi}\arccos\left(\frac{1-\frac{4Im_{min}^2}{R_1^2}}{1+\frac{4Im_{min}^2}{R_1^2}}\right) \tag{13}$$

The impedance of the diffusion part is described using Eq. 15. One has to bear in mind that the separation between transfer functions H_T and H_D holds as long as $\tau_1 << \tau_2$. At this stage, the remaining parameters (β, τ_2 and R_2) are identified using the frequential data in Eq. 14 :

$$\hat{H}_D(\Omega_D) = H_{Z,mes}(\Omega_D) - \hat{H}_T(\Omega_D) \tag{14}$$

where $\Omega_D = \{\omega_1, \ldots, \omega_{N_D}\}$ is a set of size N_D containing the frequencies in the diffusion zone and $H_{Z,mes}$ are the measured EIS data.

$$H_D(s) = \frac{R_2}{1+\tau_2 s^{\beta}} = \frac{R_2}{1+\tau_2\omega^{\beta}\cos\left(\frac{\beta\pi}{2}\right)+j\tau_2\omega^{\beta}\sin\left(\frac{\beta\pi}{2}\right)} \tag{15}$$

By computing the derivative of the imaginary part of $H_D(s)$ with respect to its real part, one gets Eq. 16 from which the value of the fractional exponent β can be retrieved using Eq. 17:

$$\frac{\partial Im(-H_D)}{\partial Re(H_D)} = \frac{(\tau_2^2\omega^{2\beta} - 1)\sin\left(\frac{\beta\pi}{2}\right)}{(\tau_2^2\omega^{2\beta} + 1)\cos\left(\frac{\beta\pi}{2}\right) + 2\omega^{\beta}\tau_2} \tag{16}$$

$$\lim_{\omega\to+\infty} \frac{\partial Im(-H_D)}{\partial Re(H_D)} = \tan\left(\frac{\beta\pi}{2}\right) \Longrightarrow \beta = \frac{2}{\pi}\arctan\left(\frac{\partial Im(-H_D)}{\partial Re(H_D)}\right) \tag{17}$$

The diffusion time constant τ_2 and impedance R_2 are obtained using the weighted linear least squares algorithm 1

Algorithm 1 Recursive weighted linear least squares.

Initialization:

$\Theta_{itr} = \begin{bmatrix} 0 & 0 \end{bmatrix}$

$$\hat{\Theta} = \underset{\tau_2,R_2}{\operatorname{argmin}} \sum_{n=1}^{N_D} \left\| \begin{bmatrix} A_1(\omega_n) & -1 \\ A_2(\omega_n) & 0 \end{bmatrix} \begin{bmatrix} \tau_2 \\ R_2 \end{bmatrix} + \begin{bmatrix} Re\left(H_D(\omega_n)\right) \\ Im\left(H_D(\omega_n)\right) \end{bmatrix} \right\|^2$$

while $\left\|\Theta_{itr} - \hat{\Theta}\right\| \leq Tol$ **do**

$\Theta_{itr} = \hat{\Theta}$

$$\hat{\Theta} = \underset{\tau_2,R_2}{\operatorname{argmin}} \sum_{n=1}^{N_D} \left\| \begin{bmatrix} \frac{A_1(\omega_n)}{W(\omega_n)} & \frac{-1}{W(\omega_n)} \\ \frac{A_2(\omega_n)}{W(\omega_n)} & 0 \end{bmatrix} \begin{bmatrix} \tau_2 \\ R_2 \end{bmatrix} + \begin{bmatrix} \frac{Re(H_D(\omega_n))}{W(\omega_n)} \\ \frac{Im(H_D(\omega_n))}{W(\omega_n)} \end{bmatrix} \right\|^2$$

end while

[45], where coefficients $A_1(\omega)$, $A_2(\omega)$ and $W(\omega)$ are computed as follows:

$$\begin{cases} A_1(\omega) &= Re\left(H_D\right)\omega^{\beta}\cos\left(\frac{\pi\beta}{2}\right) - Im\left(H_D\right)\omega^{\beta}\sin\left(\frac{\pi\beta}{2}\right) \\ A_2(\omega) &= Im\left(H_D\right)\omega^{\beta}\cos\left(\frac{\pi\beta}{2}\right) - Re\left(H_D\right)\omega^{\beta}\sin\left(\frac{\pi\beta}{2}\right) \\ W(\omega) &= \left|\left(1 + \tau_2\omega^{\beta}\cos\left(\frac{\pi\beta}{2}\right)\right)^2 + \left(\tau_2\omega^{\beta}\sin\left(\frac{\pi\beta}{2}\right)\right)^2\right|^r \\ \Theta &= \begin{bmatrix} \tau_2 & R_2 \end{bmatrix} \end{cases} \tag{18}$$

The parameter $r \in [0 \ +\infty[$ is a relaxation exponent. The increase of the value of r reduces the impact of high frequencies, which is useful given that the diffusion phenomenon occurs at low frequencies.

Using the frequency domain identification method beforehand designed designed on recorded spectroscopy data at 25 $^{\circ}C$ and $0^{o}C$, a second order FOM parameters were estimated. Figs. 2.1 and 2.2 are display identified transfer functions (dotted lines) versus measured spectroscopy data (plain lines) at $SoC \in \{100\%,\ 20\%,\ 10\%\}$ and temperatures 25 $^{\circ}C$ and 0 $^{\circ}C$. The fit is quite satisfying, and this approach provides more insight and understanding of the identified parameters values as the obtained transfer functions are mathematically fitted transfer functions.

We have established a global trend of various parameters of the model in Eq. 10 for SoC values ranging from 0% to 100% and temperature $T \in \{-15,\ 0,\ 25,\ 45\ ^{\circ}C\}$. Fig. 2.3 displays a) ohmic resistance R_0, b) fractional exponent α, c) fractional exponent β. One can notice that the ohmic resistance R_0 values increase as the SoC and the temperature

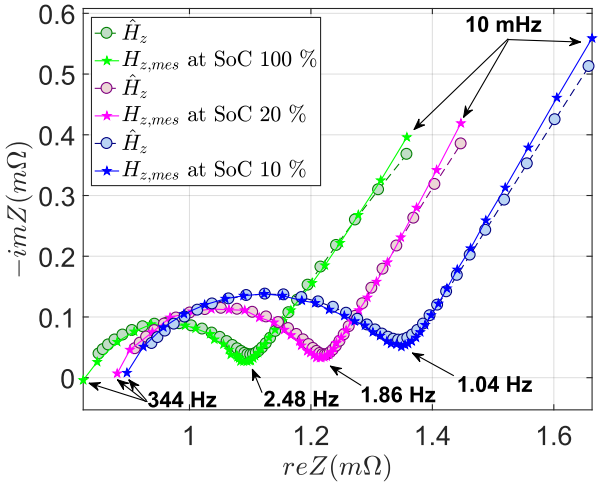

(2.1) Frequency domain identification of H_z at low SoCs at 25 °C. Identified transfer functions (dotted lines - -❍- -) versus measured spectroscopy data (plain lines -★-).

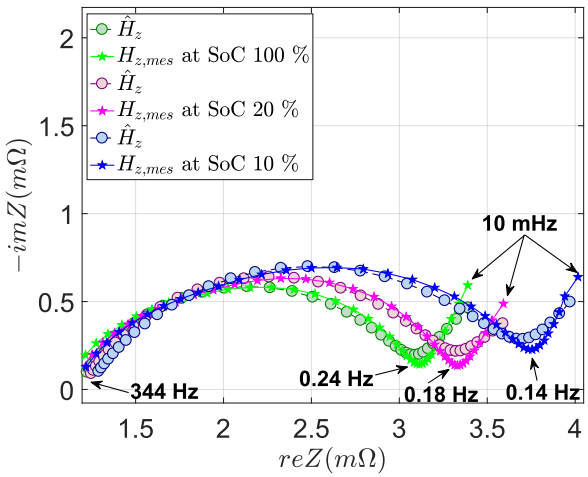

(2.2) Frequency domain identification of H_z at low SoCs at 0 °C. Identified transfer functions (dotted lines- -❍- -) versus measured spectroscopy data (plain lines -★-).

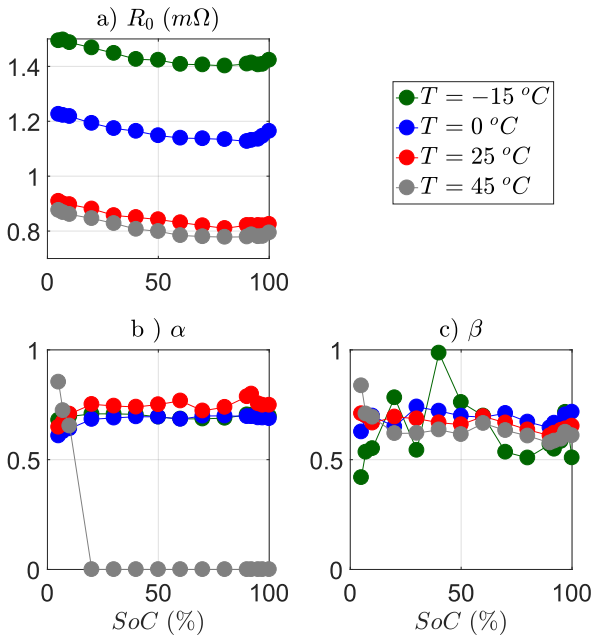

(2.3) Frequency domain identification results at different temperatures $-15,\ 0,\ 25$ and 45 °C: a) ohmic resistance R_0, b) fractional exponent α, c) fractional exponent β.

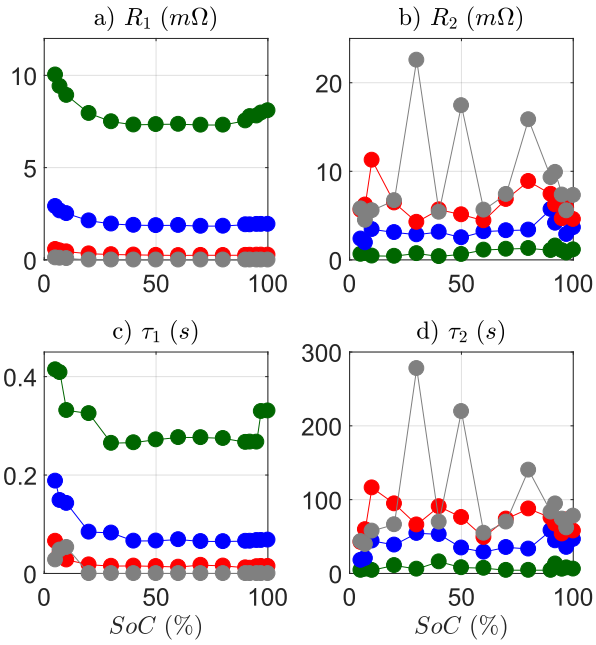

(2.4) Frequency domain identification results at different temperatures $-15,\ 0,\ 25$ and 45 °C: a) charge transfer resistance R_1, b) diffusion resistance R_2, c) charge transfer time constant τ_1, d) Diffusion time constant τ_2.

Figure 2: Frequency domain identification results

values decrease. This observation is expected given that at low temperatures, the oxydo-reduction reactions are slowed down.

Fig. 2.4 displays a) charge transfer resistance R_1, b) diffusion resistance R_2, c) charge transfer time constant τ_1, d) diffusion time constant τ_2. One can definitely notice that resistance and time constant values tend to diminish as the temperature increases. On top of that, their values rise to their maximum at low SoCs. These behaviours are expected for Li-ion batteries under these circumstances.

Neither temperature nor SoC values cause fractional exponents α and β variation. However, at 45 $^\circ C$ the displayed values of the charge transfer fractional exponent are equal to 0. The cause is the decreasing charge transfer phenomena when the temperature increases. At 45 $^\circ C$, the charge transfer phenomenon vanishes completely and appears only at lower $SoCs$. The relative fitting error was computed using Eq. 19, where Ω_{mes} is a set of size N containing all the measurement frequencies:

$$FIT(\%) = 100 \times \frac{\sum_{\omega \in \Omega_{mes}} \left| H_{z,mes}(j\omega) - \hat{H}_z(j\omega) \right|}{\sum_{\omega \in \Omega_{mes}} \left| H_{z,mes}(j\omega) \right|} \tag{19}$$

The corresponding results are displayed in Table 1. At temperatures 0, 25 and 45 $^\circ C$, the FIT values are satisfactory.

SoC	**at** $-15\ ^\circ C$	**at** $0\ ^\circ C$	**at** $25\ ^\circ C$	**at** $45\ ^\circ C$
100	79.3	93.4	97.8	97.07
97	78.3	93.28	97.8	96.66
95	82.4	93.23	97.6	96.76
92	82.2	93.10	97.7	97.17
90	82	93.11	97.6	97.16
80	83.7	92.77	97.7	97.18
70	83	92.8	97.7	96.81
60	82.6	93.36	97.2	96.53
50	82.1	93.16	97.7	97.41
40	81.3	93.16	97.8	96.86
30	82.2	91.15	97.5	97.25
20	78.7	92.14	97.4	96.26
10	81.8	89.6	97.4	96.70
7	78.8	90.82	96.4	95.86
5	80.8	89.9	94.8	93.52

Table 1: Frequency domain identification FIT values ([%]) at different temperatures.

However, at $-15\ ^\circ C$, the identification result displays a poor FIT. The frequency domain identified parameters are initial guesses for the time domain identification. Therefore, there is no urge to aspire to a 100% FIT at the current stage.

3.2. *Numerical approximation*

The simulation of a temporal domain response of a fractional order system requires all the previous output signal values. This necessity can become an issue as the memory length grows over time. For effective implementation, one can approximate the Grünwald - Letnikov definition in Eq. 4 using Eq. 20 if T_s is chosen small enough:

$$\mathcal{D}^{\alpha}x(t) = \frac{1}{T_s^{\alpha}}\sum_{j=0}^{L_m}(-1)^j C_{\alpha}^{j} x(t - jT_s) \tag{20}$$

where L_m is the "memory length" to be chosen [46]. For $|x(t)| \leq X_{max}$ (the maximal amplitude), the memory length L_m that satisfies an accuracy ξ for $\mathcal{D}^{\alpha}x(t)$ is given as [46, 47]:

$$L_m \geq \left(\frac{X_{max}}{\xi|\Gamma(1-\alpha)|}\right)^{1/\alpha} \tag{21}$$

For EV applications T_s is equal to 1 s, leading to $T_s > \tau_1$ with respect to the identified values (see Fig. 2.4-c). For example, Fig. 3.1 displays a) a one hour urban driving cycle input current $I(t)$ and b) its single-sided amplitude spectrum $|I(f)|$. The relevant excited frequencies are inferior to $2Hz$. One can recall that the estimated values of τ_1 displayed in Fig. 2.4 are less than 0.5 s. As a consequence, one can neglect the charge transfer time response.

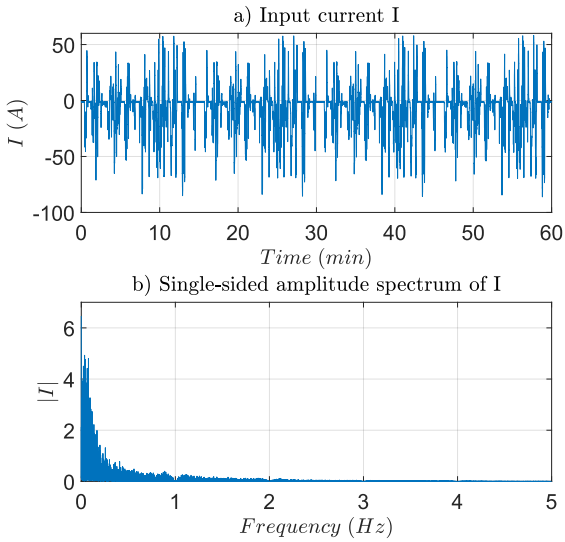

(3.1) Spectrum study of an urban driving cycle input current sampled at $T_s = 0.1$ s,at temperature 25 °C : a) Imput current $I(t)$, b) Single-sided amplitude spectrum of the current.

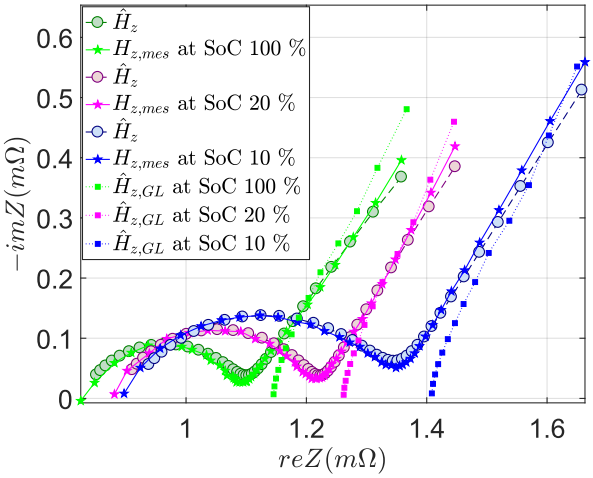

(3.2) Numerical approximation of the identified FOM transfer function with $T_s = 1$ s, at 25 °C and $L_m = 40$. Measured spectroscopy data (plain lines -★-), Identified transfers (dotted lines- -○- -) and approximation using GL (plain lines -■-).

Figure 3: GL numerical approximation based on input current spectrum.

Let's consider the fractional transfer function $H(s)$ to be identified from data sampled at $T_s > \tau_1$:

$$H_z(s) = R_{ESR} + \frac{R_2}{1 + \tau_2 s^{\beta}} \tag{22}$$

where $R_{ESR} = R_0 + R_1$ is the equivalent series resistance. The discrete transfer function corresponding to $H_z(s)$, associating z-transforms of I/O data can be written as following using GL derivatives and power series expansion:

$$H_{z,GL}(z) = R_{ECR} + \frac{R_2 T_s^\beta}{T_s^\beta + \tau_2 \sum_{k=0}^{L_m} (-1)^k C_\beta^k z^{-k}} \tag{23}$$

where z is the Z-transform variable. Fig. 3.2 displays various frequency responses, the experimental one $H_{z,mes}$, that of the identified continuous model $H_z(s)$, that of the approximate discrete model $\hat{H}_{z,GL}$ for different values of $SoC \in \{100\%;\ 20\%;\ 10\%\}$. As expected, the numerical approximation $\hat{H}_{z,GL}$ reproduces well the diffusion phenomenon whereas the charge transfer is absent.

*3.3. **Time domain identification***

The time domain identification requires the use of fractional differential Eq. 7, which one can rewrite for the studied system as follows:

$$V_z(t) = -\sum_{n=1}^{N} a_n \mathcal{D}^{\nu_{a_n}} V_z(t) + \sum_{m=0}^{M} b_m \mathcal{D}^{\nu_{b_m}} I(t) \tag{24}$$

where V_z is the voltage of the internal impedance of the battery $Z_{cell}(R_0,\ CPE_1,\ CPE_2)$, I is the input current. Using a similar approach as in [48, 49, 50], one can write a linear form of the Eq. 24 as follows:

$$V_z[k] = -\sum_{n=0}^{N} a'_n V_n^*[k] + \sum_{m=0}^{M} b'_m I_m^*[k] \tag{25}$$

where:

$$a'_n = a_n \left(\sum_{i=0}^{N} a_i T_s^{\nu_{a_n} - \nu_{a_i}} \right)^{-1} \tag{26a}$$

$$b'_m = b_m \left(\sum_{i=0}^{N} a_i T_s^{\nu_{b_m} - \nu_{a_i}} \right)^{-1} \tag{26b}$$

$$V_n^*[k] = \sum_{i=1}^{k} (-1)^i C_{\nu_{a_n}}^i V_z[k-i] \tag{26c}$$

$$I_m^*[k] = \sum_{i=0}^{k} (-1)^i C_{\nu_{b_m}}^i I[k-i] \tag{26d}$$

One can then notice that $\sum_{n=0}^{N} a'_n = 1$ using Eq. 26. Thus, the number of estimated parameters can be reduced by one, and the linear Eq. 25 becomes:

$$\hat{V}_z[k, \hat{\theta}_r] = -V_0^*[k] - \sum_{n=1}^{N} \hat{a}'_n (V_n^*[k] - V_0^*[k]) + \sum_{m=0}^{M} \hat{b}'_m I_m^*[k] \tag{27}$$

where $\hat{\theta}_r = [\hat{a}'_1\ \hat{a}'_2\ \dots\ \hat{a}'_N\ \hat{b}'_0\ \hat{b}'_1\ \dots\ \hat{b}'_M]$ is the parameter vector. Noting the estimated output $\hat{y}[k] = \hat{V}_z[k, \hat{\theta}_r] + V_0^*[k]$, parameters $\hat{\theta}_r$ can be estimated using an instrumental variable recursive least square (IV-RLS) algorithm with

a forgetting factor laid down in Eq. 28:

$$\hat{\theta}_r[k] = \hat{\theta}_r[k-1] + L[k]\left[y[k] - \hat{\theta}_r^T[k-1]\phi[k]\right], \tag{28a}$$

$$L[k] = \frac{P[k-1]\phi^{IV}[k]}{\lambda + \phi^T[k]P[k-1]\phi^{IV}[k]}, \tag{28b}$$

$$P[k] = \frac{1}{\lambda}(P[k-1] - L[k]\phi[k]P[k-1]) \tag{28c}$$

where $0 << \lambda \leq 1$ is the forgetting factor, $L[k]$ is the correction gain vector, $P[k]$ the error covariance matrix at time index k, and the measurement vectors ϕ, ϕ^{IV} are given in Eq. 29 [24]:

$$\phi = \left[-(V_1^* - V_0^*) \ \ldots \ -(V_N^* - V_0^*)\ I_0^* \ \ldots \ I_M^*\right]^T \tag{29a}$$

$$\phi^{IV} = \left[-(V_1^* - V_0^*)^{IV} \ \ldots \ -(V_N^* - V_0^*)^{IV}\ I_0^* \ \ldots \ I_M^*\right]^T \tag{29b}$$

Φ^{IV} is computed at each iteration using the output obtained by simulating the model with estimated parameters from the previous iteration. One can retrieve the initial parameters: a_l and b_m using Eqs. 30 and 31 [49, 48]:

$$\begin{cases} \left[a_1' T_s^{\nu_{a_0}} \quad \ldots \quad a_N' T_s^{\nu_{a_0}}\right]^T = \mathcal{M} \times \left[a_1 \quad \ldots \quad a_N\right]^T \\ \mathcal{M} = \begin{bmatrix} \frac{(1-a_1')}{T_s^{\nu_{a_1}}} & -a_1' T_s^{-\nu_{a_2}} & \ldots & -a_1' T_s^{-\nu_{a_N}} \\ -a_1' T_s^{-\nu_{a_1}} & \frac{(1-a_2')}{T_s^{\nu_{a_2}}} & \ldots & -a_1' T_s^{-\nu_{a_N}} \\ \vdots & \vdots & \vdots & \vdots \\ -a_N' T_s^{-\nu_{a_1}} & -a_N' T_s^{-\nu_{a_2}} & \ldots & \frac{(1-a_N')}{T_s^{\nu_{a_N}}} \end{bmatrix} \end{cases} \tag{30}$$

$$b_m = b_m' \sum_{n=0}^{N} a_n T_s^{\nu_{b_m} - \nu_{a_n}} \tag{31}$$

In the present study case, considering the transfer model in Eq. 22; the set of parameters and equations is given as following:

$$a = \begin{bmatrix} 1 & \tau_2 \end{bmatrix} \qquad \nu_a = \begin{bmatrix} 0 & \beta \end{bmatrix} \tag{32a}$$

$$b = \begin{bmatrix} R_2 + R_{ESR} & \tau_2 R_{ESR} \end{bmatrix} \qquad \nu_b = \begin{bmatrix} 0 & \beta \end{bmatrix} \tag{32b}$$

$$\theta_r = \begin{bmatrix} a_1' & b_0' & b_1' \end{bmatrix} \tag{32c}$$

$$\hat{a}_1 = \frac{\hat{a}_1'}{(1 - \hat{a}_1') T_s^{-\beta}} \tag{32d}$$

$$\hat{b}_0 = \hat{b}_0'(\hat{a}_0 + \hat{a}_1 T_s^{\beta}) \qquad \hat{b}_1 = \hat{b}_1'(\hat{a}_0 T_s^{\beta} + \hat{a}_1) \tag{32e}$$

To asses the presented method, there are two types of time domain test that were run. First the current pulse excitations of the battery at various SoCs; and secondly, driving cycle current profile applied to the battery. Those tests are detailed in the following subsections.

3.3.1. *Current pulse excitation*

For this test, an EV Li-ion battery with a charge capacity $Q_n = 64\ Ah$ is considered. Pulsed currents of $1C$ amplitude ($64\ A$) for about 2 mins and an imposed relaxation of about 8 minutes were utilized as inputs. Knowing the SoC of this cell, one can easily compute its internal impedance voltage using Eq. 33. The transfer $H_z(s)$ between $V_z(s)$ and $I(s)$ can be identified using an adaptive IV-RLS algorithm with a forgetting factor λ. To enable rapid convergence of the time domain identification, the initial guess of parameters τ_2, R_2 and R_{ESR} are derived from the frequency domain identification result using the model in Eq. 22:

$$V_z[k] = V_t[k] - OCV(SoC[k]) \tag{33}$$

Fig. 4.1 displays a) the reference SoC, b) the pulsed current, and the internal impedance voltage obtained using Eq. 33.

Knowing that the SoC is near 20%, the initial guess transfer function was obtained using the frequency domain result at $SoC = 20\%$ from section 3.1. A lower bound of the "memory length" can be computed using Eq. 21. For example, if $V_{z,max} = 400\ mV$ and $\beta = 0.7$; to achieve a $10\ mV$ accuracy : L_m must be superior to 40. For simplicity the memory length is chosen as $L_m = \lfloor T/T_s \rfloor$; where T is a time constant to be chosen at least superior to the response time of the system. The accuracy of the numerical approach will improve as the value of T increases. Unfortunately, the memory length required for the computation also increases, consequently increasing the computational time. Fig. 4.2 displays the results for two distinctive values of the time constant $T \in \{120\ s, 600\ s\}$.

Similarly at $0\ ^\circ C$ around $SoC = 30\%$ the same test was conducted leading to the result displayed in Fig. 4.3.

Errors	**FOM:** $L_m = 120$	**FOM:** $L_m = 600$	**EEC**
RMS, **at** ($SoC = 20\%$, $25\ ^\circ C$)	7.01	3.11	10.02
Max, **at** ($SoC = 20\%$, $25\ ^\circ C$)	11	10.98	14.66
RMS, **at** ($SoC = 30\%$, $0\ ^\circ C$)	15.82	8.8	22.02
Max, **at** ($SoC = 30\%$, $0\ ^\circ C$)	24.51	12.71	30.95

Table 2: Voltage estimation error for pulsed current inputs at $25\ ^\circ C$ and $0\ ^\circ C$

In both of these figures, one can clearly confirm that FOM results are more accurate than first order equivalent circuit model. Also the increase of the value of T improves the accuracy as displayed in Table 2. However, to limit the computational burden, the value of T will not be increased too considerably.

3.3.2. *Driving cycle excitation*

For this test, recorded driving cycle data were used as inputs of the proposed model. Knowing the SoC the same scheme and Eq. 33 were utilized to retrieve voltage V_z of internal impedance of the battery displayed on Fig. 5.1. The transfer function $H_z(s)$ between $V_z(s)$ and $I(s)$ can be identified implementing an adaptive RLS algorithm with a

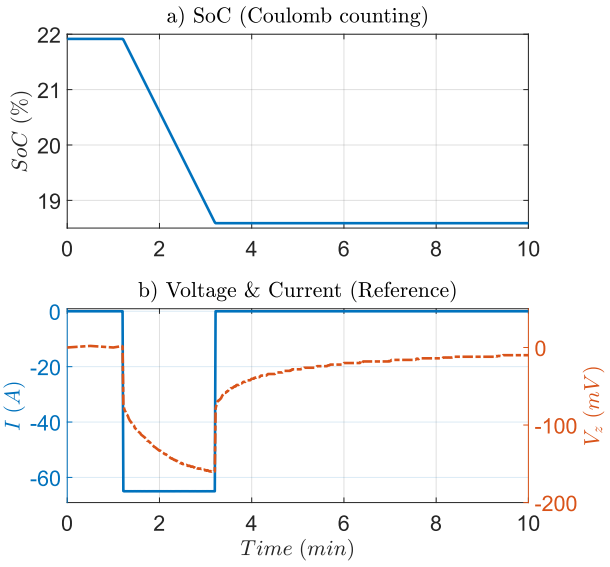

(4.1) Input data for a $Q_n = 64\ Ah$ cell at 25 $^\circ C$ a) State of Charge b) (left) Applied pulsed current and (right) internal impedance voltage obtained using Eq. 33 ($T_s = 1\ s$).

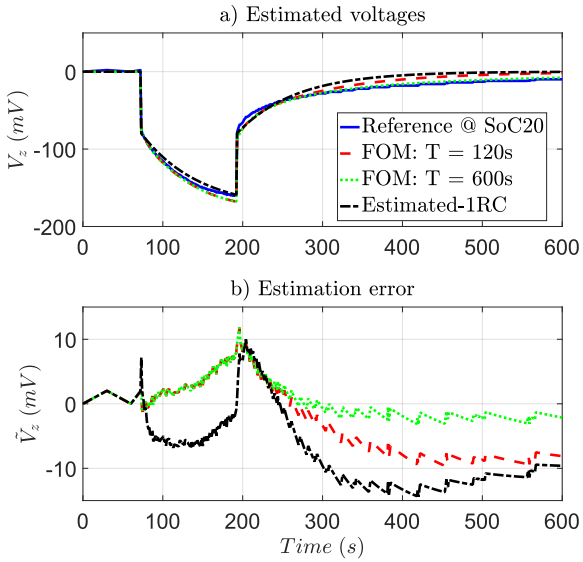

(4.2) a) Estimated Voltage b) Estimation error for a $Q_n = 64\ Ah$ charge capacity cell, around 20% SoC at 25 $^\circ C$ ($T_s = 1\ s$, $L_m = \lfloor T/T_s \rfloor$).

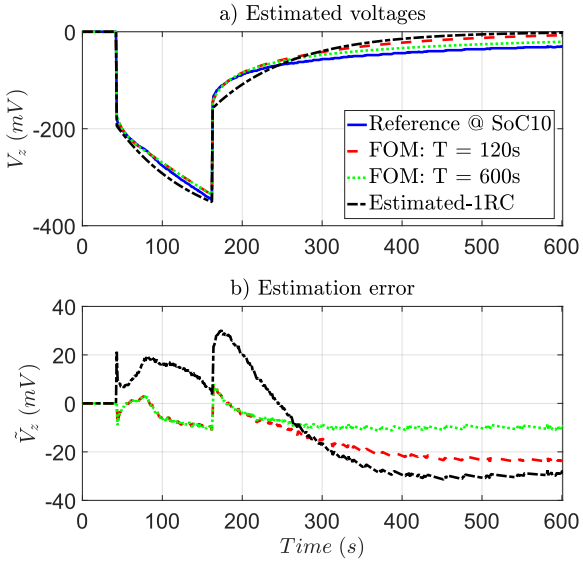

(4.3) a) Estimated Voltage b) Estimation error for a $Q_n = 64\ Ah$ charge capacity cell, around 30% SoC at 0 $^\circ C$ ($T_s = 1\ s$, $L_m = \lfloor T/T_s \rfloor$).

Figure 4: Parameters identification for a pulsed current excitation.

forgetting factor λ. On Fig. 5.2 are displayed the estimated voltages and the estimation errors for both FOM and first order EEC model.

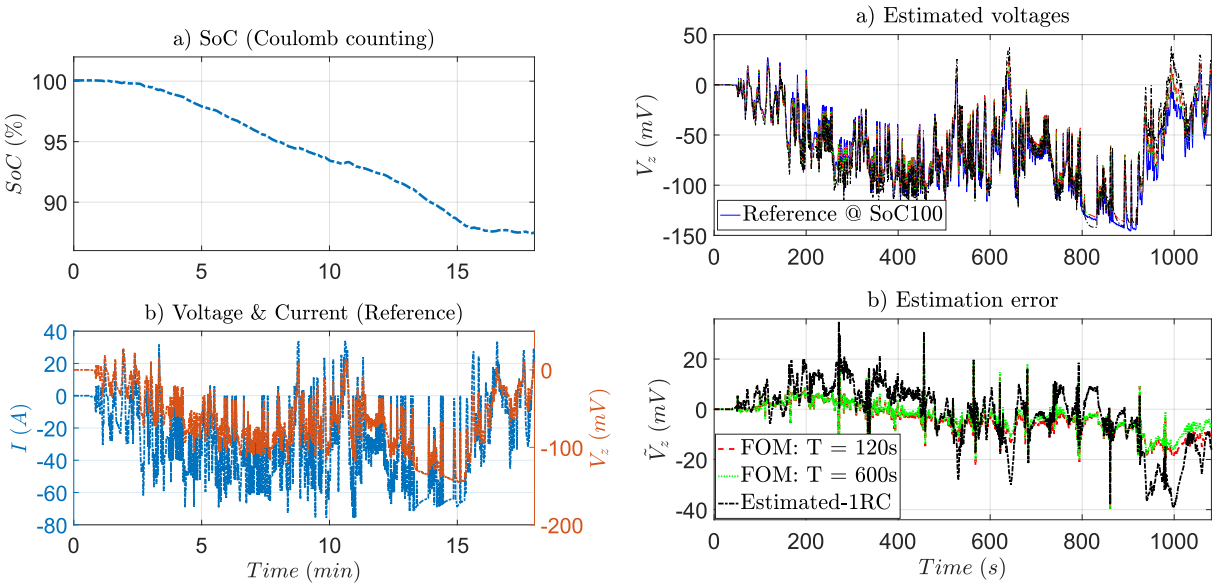

(5.1) Input data for a $Q_n = 64\ Ah$ cell at 25 $°C$ for highway driving cycle a) State of Charge b) (left) Applied pulsed current and (right) internal impedance voltage obtained using Eq. 33 ($T_s = 1\ s$).

(5.2) a) Estimated Voltage b) Estimation error for a $Q_n = 64\ Ah$ charge capacity cell, for SoC ranging from 100% to 87% at 25 $°C$ ($T_s = 1\ s$, $L_m = \lfloor T/T_s \rfloor$).

Figure 5: Parameters identification for a driving cycle excitation.

As observed for current pulse excitations, when using the FOM, the estimation errors are reduced in comparison to first order EEC model. Also the increase of the value of T improves the accuracy of the identification. The error comparison is displayed in table 3. It is essential to notice that in this case, there is no need to increase significantly the value of L_m. This is cause by the fact that the input current does not excite low frequencies very much.

Errors	**FOM:** $L_m = 30$	**FOM:** $L_m = 300$	**EEC**
$RMS\ (mV)$	8.94	7.59	12.49
$Max\ (mV)$	37.99	37.49	39.01

Table 3: Voltage estimation error comparison for a highway driving cycle and SoC ranging from 100% to 87% at 25 $°C$ ($T_s = 1\ s$, $L_m = \lfloor T/T_s \rfloor$).

4. Fractional-order-EKF for Li-ion batteries

The aim in this section is to design and test an extended Kalman observer based on FOM for Li-ion batteries. First, a generalized filter for a second order FOM will be designed. Following that, the filter will be adapted to the presented study case.

4.1. *Filter design*

Differential equation describing the evolution of the voltages of the constant phase elements (CPEs) displayed in Fig. 1.1 is given as:

$$\mathcal{D}^{\alpha_i} V_{CPE,i}(t) = -\frac{1}{\tau_i} V_{CPE,i}(t) + \frac{R_i}{\tau_i} I(t) \tag{34}$$

where $\alpha_i \in \{\alpha,\ \beta\}$. Eq. 34 leads to the discrete time Eq. 35, using numerical approximation of the Grünwald-Letnikov fractional derivative displayed in Eq. 20:

$$\mathcal{D}^{\alpha_i} V_{CPE,i}[k+1] = \frac{1}{T_s^{\alpha_i}} \{V_{CPE,i}[k+1] + \sum_{j=1}^{L_m} (-1)^j C_{\alpha_i}^j V_{CPE,i}[k+1-j]\} \tag{35}$$

This allows the computation of the CPE voltage at time index k, as linear combination of its previous values and the input current value $I[k]$:

$$V_{CPE,i}[k+1] = \left(\alpha_i - \frac{T_s^{\alpha_i}}{\tau_i}\right) V_{CPE,i}[k] - \sum_{j=2}^{L_m} (-1)^j C_{\alpha_i}^j V_{CPE,i}[k+1-j] + \frac{R_i T_s^{\alpha_i}}{\tau_i} I[k] \tag{36}$$

For each CPE, one can consider the state vector to be:

$$x_i[k] = [V_{CPE,i}[k],\ V_{CPE,i}[k-1],\ \ldots,\ V_{CPE,i}[k+1-L_m]]^T \tag{37}$$

The state equation of one CPE is computed as follows:

$$x_i[k+1] \quad = \quad A_i x_i[k] + B_i I[k] \tag{38}$$

where

$$\begin{cases} A_i & = & \begin{bmatrix} \alpha_i - \frac{T_s^{\alpha_i}}{\tau_i} & W_2 & W_3 & \ldots & W_{L_m} \\ 1 & 0 & 0 & \ldots & 0 \\ 0 & 1 & 0 & \ddots & \vdots \\ \vdots & \ddots & \ddots & \ddots & 0 \\ 0 & \ldots & 0 & 1 & 0 \end{bmatrix} \\ B_i & = & \begin{bmatrix} \frac{R_i T_s^{\alpha_i}}{\tau_i} & 0 & \ldots & 0 \end{bmatrix}^T \\ W_j & = & (-1)^{j+1} C_{\alpha_i}^j \end{cases} \tag{39}$$

Considering the SoC definition in Eq. 40, one writes the global state equation of the system using Eq. 41:

$$SoC[k+1] = SoC[k] + \frac{I[k] T_s}{Q_n \times 3600} \tag{40}$$

$$x[k+1] = Ax[k] + BI[k] \tag{41a}$$

$$V_t[k] = \sum_{i=1}^{2} V_{CPE,i}[k] + OCV(SoC[k]) + R_0 I[k] \tag{41b}$$

where:

$$\begin{cases} A & = & \begin{bmatrix} A_1 & 0_{L_m \times L_m} & 0_{L_m \times 1} \\ 0_{L_m \times L_m} & A_2 & 0_{L_m \times 1} \\ 0_{1 \times L_m} & 0_{1 \times L_m} & 1 \end{bmatrix} \\ B & = & \begin{bmatrix} B_1 & B_2 & T_s/(3600 \times Q_n) \end{bmatrix}^T \\ x[k] & = & \begin{bmatrix} x_1[k] & x_2[k] & SoC[k] \end{bmatrix}^T \end{cases} \tag{42}$$

$A \in \mathbb{R}^{(2*L_m+1)\times(2*L_m+1)}$, $B \in \mathbb{R}^{(2*L_m+1)\times 1}$, $B \in \mathbb{R}^{1\times(2*L_m+1)}$ and V_t is the terminal voltage of the battery. The function $OCV(SoC)$ is an optimized lookup table provided by the manufacturer of the Li-ion batteries used in this paper. Similar solutions were adopted in the literature. For example, in [51] a fractional Kalman filter was derived based on a simplified electrochemical model. Whereas, in [36] an unscented Kalman filter (UKF) was designed for SoC estimation while the parameters were estimated using a genetic algorithm. In [27] a sliding mode observer was designed based on frequency domain identification using particle swarm optimization (PSO). A multi-swarm cooperative particle swarm optimization (MCPSO) is used to identify fractional order parameters while the SoC was estimated using an EKF in [26]. This paper proposes a simple EKF based SoC estimation with a FOM derived from a new frequency domain data identification for Li-ion batteries. The EKF algorithm steps are given below:

Prediction:

$$\hat{x}^-[k] = A\hat{x}[k-1] + BI[k-1], \tag{43a}$$

$$P_x^-[k] = AP_x^+[k-1]A^T + Q_x. \tag{43b}$$

Update:

$$L_x[k] = P_x^-[k]C^T \left[CP_x^-[k]C^T + R\right]^{-1}, \tag{43c}$$

$$\hat{x}^+[k] = \hat{x}^-[k] + L_x[k]\left[V_t[k] - C\hat{x}^-[k] - DI[k]\right], \tag{43d}$$

$$P_x^+[k] = P_x^+[k-1] - L_xCP_x^-[k]. \tag{43e}$$

where P_x^- and P_x^+ are the predicted and updated state error covariance matrix, Q_x and R the state and measurement noises covariance matrix, L_x the correction gain matrix; C and D are given in the following equation:

$$\begin{cases} C & = & \begin{bmatrix} 1 & 0 & \dots & 1 & 0 & \dots & \frac{\partial OCV}{\partial SoC}|_{SoC[k-1]} \end{bmatrix} \\ D & = & R_0 \end{cases} \tag{44}$$

Using Eq. 41 jointly with the parameter estimator described in Section 3.3, one can estimate the SoC of the Li-ion cell as displayed Fig. 6.1. It is a dual estimator scheme [9] with an RLS component that estimates the FOM model parameters using measured currents $\begin{bmatrix} I[k] & I[k-1] \end{bmatrix}$ and the estimated state of charge $S\hat{o}C[k-1]$. A convergence test is run to retrieve converged parameters $R_{0,conv}$, $(\tau_1,\ R_1)_{conv}$ and $(\tau_2,\ R_2)_{conv}$. These converged parameters are then used by the EKF observer to build matrix A, B, C and D when estimating the state vector: $x[k] = \begin{bmatrix} x_1[k] & x_2[k] & SoC[k] \end{bmatrix}^T$, of size $2 \times L_m + 1$.

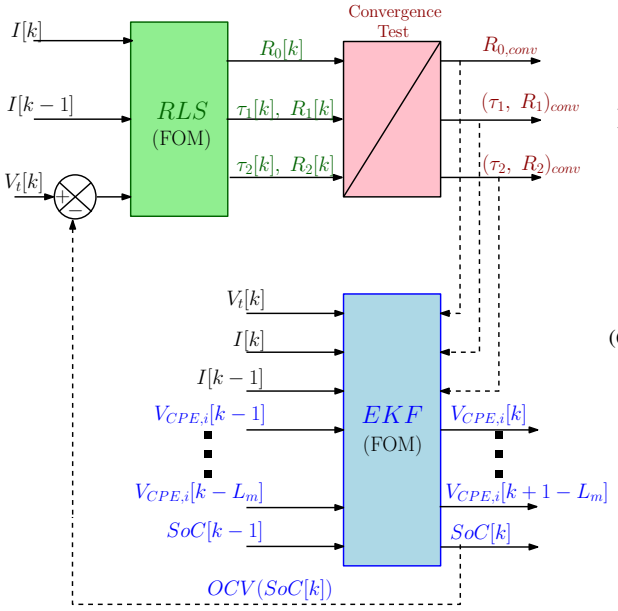

(6.1) Dual filter diagram for SoC and parameters estimation.

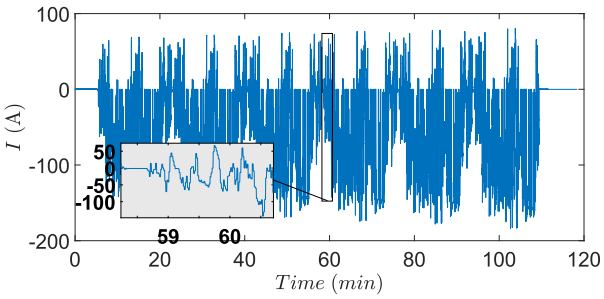

(6.2) Highway driving cycle input current at 25 °C (Experimental data).

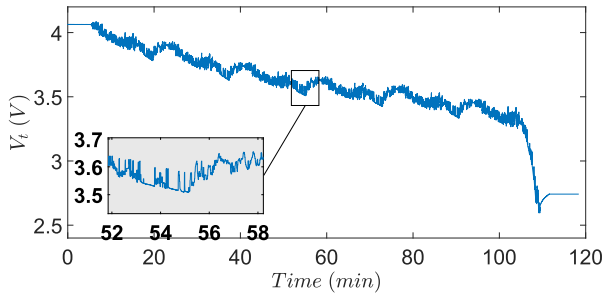

(6.3) Highway driving cycle output voltage at 25 °C. (Experimental data).

Figure 6: GL numerical approximation based on input current spectrum.

4.2. ***Experimentation***

Considering the model in Eq. 22 where only one CPE is used, the state of the proposed fractional EKF is $x[k] = \begin{bmatrix} x_2[k] & SoC[k] \end{bmatrix}^T$ of size $L_m + 1$, and the parameters to be estimated are R_{ESR}, R_2 and τ_2. Using the presented dual filter scheme and data recorded from a Li-ion cell during highway driving cycle at 25 °C, both SoC and parameters of the first order FOM were estimated for a Li-ion cell. Fig. 6.2 displays the input current whereas Fig. 6.3 displays the output voltage.

For this test $L_m = 40$, $T_s = 1\ s$, $\beta = 0.66$. Noting b_I and b_V the additive current and voltage measurement noises in Eq. 45, one can easily compute the noise covariance matrices using Eq. 46:

$$\begin{cases} V_{t,mes} &= V_t + b_V \\ I_{mes} &= I + b_I \end{cases} \tag{45}$$

$$\begin{cases} Q_x &= \sigma^2_{b_I} \times BB^T \\ R &= \sigma^2_{b_I} \times R^2_{ESR} + \sigma^2_{b_V} \end{cases} \tag{46}$$

where $\sigma^2_{b_I} = 10^{-4}A^2$ and $\sigma^2_{b_V} = 10^{-7}V^2$ are the current and voltage measurement noise variances. Those noises are considered to be additive and of zero mean and white.

Fig. 7.1 displays a) the reference state of charge SoC_{ref} (blue plain line) and the estimated state of charge $S\hat{o}C$ (dotted blue line), b) the estimation error $S\tilde{o}C$ (red plain line). Fig. 7.2 displays a) the estimated diffusion time constant τ_2, b) the estimated diffusion resistance R_2 (right) and the Equivalent series resistance R_{ESR} (left). One can notice the increase of τ_2 and R_2 values as the state of charge decreases.

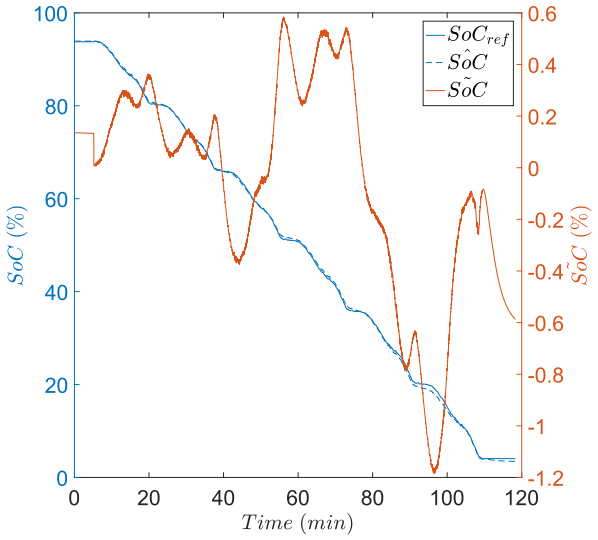

(7.1) State of charge: Reference SoC_{ref} (blue plain line), estimated $S\hat{o}C$ (dotted blue line) and the error $S\tilde{o}C$ (red plain line).

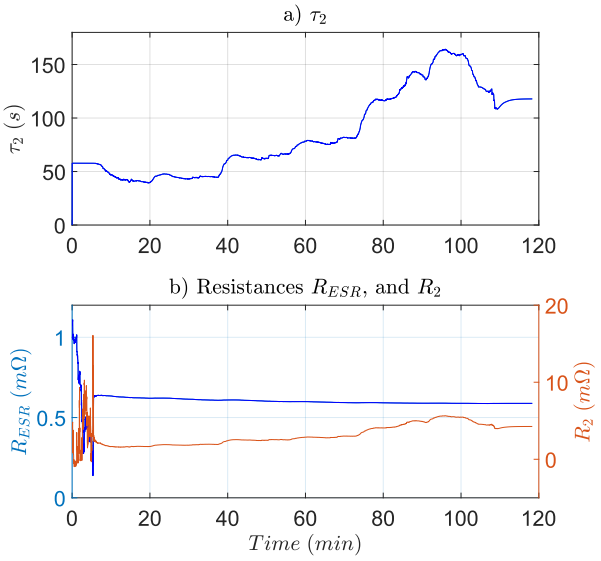

(7.2) Estimated parameters: a) Diffusion time constant τ_2, b)(right) Diffusion resistance R_2, (left) Equivalent series resistance R_{ESR}.

Figure 7: Estimated State of charge and parameters for a highway driving cycle input current at 25 $^{\circ}C$.

In table 4 are displayed SoC estimation errors using FOM and first-order EEC. As expected, the use of the FOM model leads to lower SoC estimation error values, justifying the use of FOM for Li-ion batteries. To go even further,

Errors	**1//RC (EEC Model)**	**1R//CPE (FOM)**
$RMS(\%)$	0.58	0.41
$Max(\%)$	1.86	1.18

Table 4: SoC estimation error comparison for a highway driving cycle input current at $25^{o}C$

several driving profiles were computed, at temperatures 0 $^{\circ}C$ and 25 $^{\circ}C$ using FOM and EEC on not only EV but also a PHEV battery. The SoC estimation errors comparison is displayed in Tables 5 and 6. For both EV and PHEV profiles one can notice that all RMS and maximum errors are improved when using FOM models. In addition, the maximum error improvement at low temperature is more significant. The averaged improvement of the SoC maximum error for all PHEV profiles at 25 $^{\circ}C$ is about 1% compared to 2.5% at 0 $^{\circ}C$. This can be explained by a more pronounced non-linear behaviour of Li-ion batteries at low temperatures. All these improvements justify the use of the FOM for

SoC estimation. The several driving cycles used as input for the tests in Tables 5 and 6 are displayed in Figs. 8.1, 8.2

Profiles	25 °C					0 °C				
	FOM		EEC		**SoC range**	FOM		EEC		**SoC range**
	Max (%)	*RMS* (%)	*Max* (%)	*RMS* (%)		*Max* (%)	*RMS* (%)	*Max* (%)	*RMS* (%)	
Urban	1.15	1.12	1.35	1.9	90 - 0	0.8	0.43	1.41	0.68	93 - 6
Highway	1.18	0.41	1.86	0.58	94 - 3.5	0.94	0.47	1.82	1.15	90 - 1

Table 5: SoC estimation error comparison for several driving profiles for an EV battery of charge capacity $Q_n = 64\ Ah$, $L_m = 40$.

Profiles	25 °C					0 °C				
	FOM		EEC		**SoC range**	FOM		EEC		**SoC range**
	Max (%)	*RMS* (%)	*Max* (%)	*RMS* (%)		*Max* (%)	*RMS* (%)	*Max* (%)	*RMS* (%)	
NEDC	0.34	0.18	1.44	1	94 - 6	1.8	1.3	4.54	3	94 - 12
Urban	2.1	1.42	3.61	2.27	100 - 40	6.58	3.65	7.27	3.9	92 - 9
Road	1.44	0.71	2.25	1.18	91 - 6	1.92	0.84	5.3	3.2	91 - 7
Highway	0.82	0.397	0.82	0.68	91 - 40	1.07	0.45	3.5	2.27	92 - 4.6

Table 6: SoC estimation error comparison for several driving profiles for a PHEV battery, $L_m = 40$.

and 8.3 for the convenience of the reader.

In this paper, the proposed method (FOM) is compared to the existing method (EEC) using single cells. Out of the 12 tests performed (8 PHEV tests and 4 EV tests), the execution time ration between FOM and EEC approach is about 1.68 with a standard deviation of 0.066. EVs and PHEVs frequently feature several (up to $N = 100$) cells organized in modules (or stacks). Increasing the computational time by 68% can therefore be challenging.

Globally, a compromise should be considered between increasing estimator complexity leading to increased time and resources consumption, and on the other hand, improving battery state accuracy benefits. Electrified vehicles are continuously challenged, that's why more accuracy could be important in extending autonomy range, charging time optimization and even more precise understanding of battery degradation. That is why the suggested approach must be considered in a broader framework. In fact, in [52] the "Bar-Delta" approach was proposed to reduce the CPU load for battery pack state estimation. It was argued that in the battery pack only the limiting cells (most charged during charge and least charged during discharge) are relevant. This CPU reduction strategy can be combined with the proposed FOM for the limiting cells. In doing so, the overall CPU load is reduced in comparison with the direct approach consisting of N different EEC based EKFs. On top of that, the accuracy is improved for the limiting cells thanks to the FOM approach, as suggested in the present paper.

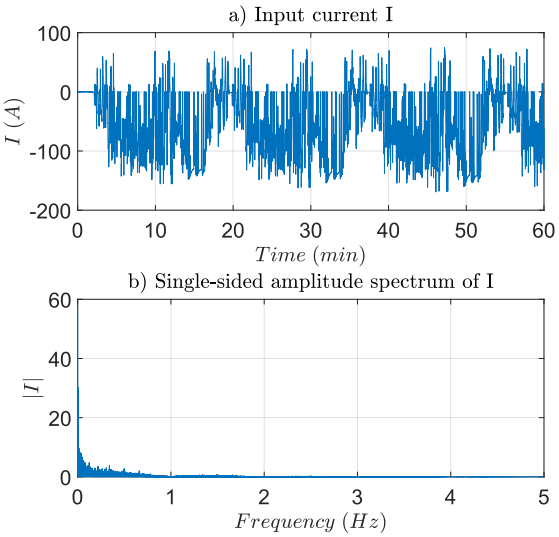

(8.1) Spectrum study of a Highway driving cycle input current sampled at $T_s = 0.1\ s$,at temperature 25 $°C$: a) input current $I(t)$, b) Single-sided amplitude spectrum of the current.

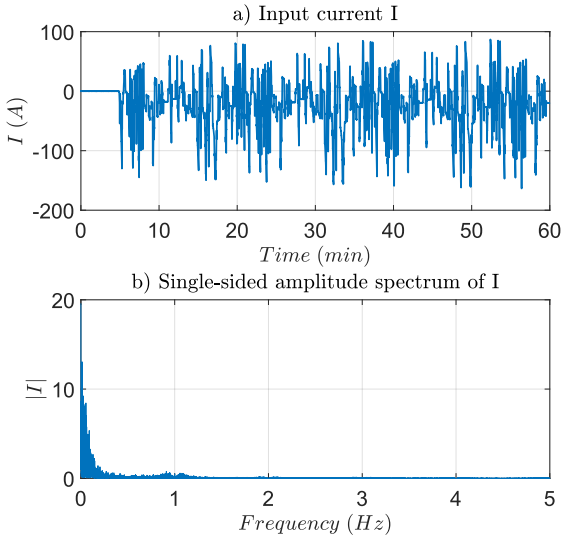

(8.2) Spectrum study of a countryside road driving cycle input current sampled at $T_s = 0.1\ s$,at temperature 25 $°C$: a) input current $I(t)$, b) Single-sided amplitude spectrum of the current.

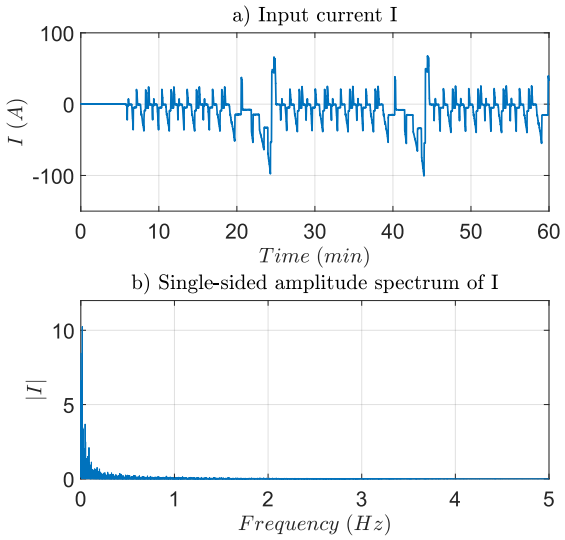

(8.3) Spectrum study of an NEDC driving cycle input current sampled at $T_s = 0.1\ s$,at temperature 25 $°C$: a) input current $I(t)$, b) Single-sided amplitude spectrum of the current.

Figure 8: Driving cycle input current used in this paper.

5. Conclusion

A method to estimate a second order fractional model parameters for Li-ion batteries using recorded EIS data for an EV and PHEV Li-ion batteries was presented in this paper. The proposed identification approach is original. The studied FOM parameters are simply and efficiently identified by taking advantage of the structure of the proposed model. Frequency domain estimation results were used to initialize the time domain estimation for pulsed and driving cycle current inputs, which enabled fast convergence and good estimation results. The study suggests that FOM is more suitable than the classical integer order systems for Li-ion batteries SoC estimation. To that extent, a joint estimator for FOM parameters and the state of charge SoC was then presented. The parameters are estimated using an IV-RLS while the battery SoC is estimated using a FOM-EKF. The designed fractional-order filter provides a higher accuracy level in comparison to the classical one based on the integer order model, therefore fulfilling the requirement of SoC accuracy improvement. The improved model enables a better behaviour understanding and could be helpful for ageing mechanism investigation. For example, using the identified model parameter, all along the life, ageing law and SoH could be predicted.

Nomenclature

Abbreviations

BMS Battery management system

CPE Constant phase element

EEC Equivalent electric circuit

EIS Electrochemical impedance spectroscopy

EKF Extended Kalman filter

EV Electric vehicle

FOC Fractional order calculus

FOM Fractional order model

FOT Fractional order transfer

HEV Hybrid electric vehicle

IV-RLS Instrumental variable - recursive least square

NEDC New european driving cycle

OCV	Open circuit voltage
PDE	Partial diferential equation
PHEV	Plug-in hybrid electric vehicle
RLS	Recursive least square
SoC	State of charge

Math Symbols

α	First CPE fractional exponent	$\in [0,\ 1]$
α_i	i-th fractional exponent	$\in [0,\ 1]$
β	Second CPE fractional exponent	$\in [0,\ 1]$
λ	Adaptive forgetting factor	$\in]0,\ 1]$
$\mathcal{D}^{\alpha}$	Fractional derivative of order α	
ω	Angular frequency	rad/s
τ_i	Time constant of the i-th CPE	s
H_z	Transfer function of the internal impedance of the cell	
I	Current of the cell	A
$Im(.)$	Imaginary part of complex number	
L_m	Memory length	
Q_n	Nominal charge capacity	Ah
R_0	Ohmic resistance	Ω
R_i	i-th resistance	Ω
R_{ESR}	Equivalent series resistance	Ω
$Re(.)$	Real part of complex number	
T	Time span	s
T_s	Sampling time	s

V_z	Voltage of the internal impedance of the cell	V
$V_{CPE,i}$	Voltage of the i-th CPE	V
V_t	Terminal voltage of the cell	V

References

[1] Boucar Diouf and Christophe Avis. The potential of Li-ion batteries in ECOWAS solar home systems. *Journal of Energy Storage*, 22:295–301, April 2019.

[2] Shruti Suriyakumar, Sivalingam Gopi, Murugavel Kathiresan, Suriyasarathi Bose, E. Bhoje Gowd, Jijeesh R. Nair, Natarajan Angulakshmi, Giuseppina Meligrana, Federico Bella, Claudio Gerbaldi, and A. Manuel Stephan. Metal organic framework laden poly(ethylene oxide) based composite electrolytes for all-solid-state Li-S and Li-metal polymer batteries. *Electrochimica Acta*, 285:355–364, September 2018.

[3] Kazunori Takada. Progress in solid electrolytes toward realizing solid-state lithium batteries. *Journal of Power Sources*, 394:74–85, August 2018.

[4] Jun Zhang, Chao Zheng, Jiatao Lou, Yang Xia, Chu Liang, Hui Huang, Yongping Gan, Xinyong Tao, and Wenkui Zhang. Poly(ethylene oxide) reinforced Li6ps5cl composite solid electrolyte for all-solid-state lithium battery: Enhanced electrochemical performance, mechanical property and interfacial stability. *Journal of Power Sources*, 412:78–85, February 2019.

[5] Rui Xiong, Linlin Li, and Jinpeng Tian. Towards a smarter battery management system: A critical review on battery state of health monitoring methods. *Journal of Power Sources*, 405:18–29, November 2018.

[6] Xiaoyu Li, Zhenpo Wang, Lei Zhang, Changfu Zou, and David. D. Dorrell. State-of-health estimation for Li-ion batteries by combing the incremental capacity analysis method with grey relational analysis. *Journal of Power Sources*, 410-411:106–114, January 2019.

[7] Yi Li, Mohamed Abdel-Monem, Rahul Gopalakrishnan, Maitane Berecibar, Elise Nanini-Maury, Noshin Omar, Peter van den Bossche, and Joeri Van Mierlo. A quick on-line state of health estimation method for Li-ion battery with incremental capacity curves processed by Gaussian filter. *Journal of Power Sources*, 373:40–53, January 2018.

[8] M. Lucu, E. Martinez-Laserna, I. Gandiaga, and H. Camblong. A critical review on self-adaptive Li-ion battery ageing models. *Journal of Power Sources*, 401:85–101, October 2018.

[9] Gregory L. Plett. Extended Kalman filtering for battery management systems of LiPB-based HEV battery packs: Part 1. Background. *Journal of Power Sources*, 134(2):252–261, August 2004.

[10] Yuejiu Zheng, Minggao Ouyang, Xuebing Han, Languang Lu, and Jianqiu Li. Investigating the error sources of the online state of charge estimation methods for lithium-ion batteries in electric vehicles. *Journal of Power Sources*, 377:161–188, February 2018.

[11] Akram Eddahech, Olivier Briat, and Jean-Michel Vinassa. Performance comparison of four lithium–ion battery technologies under calendar aging. *Energy*, 84:542–550, May 2015.

[12] J. Vetter, P. Novák, M. R. Wagner, C. Veit, K. C. Möller, J. O. Besenhard, M. Winter, M. Wohlfahrt-Mehrens, C. Vogler, and A. Hammouche. Ageing mechanisms in lithium-ion batteries. *Journal of Power Sources*, 147(1):269–281, September 2005.

[13] Jinhao Meng, Mattia Ricco, Anirudh Budnar Acharya, Guangzhao Luo, Maciej Swierczynski, Daniel-Ioan Stroe, and Remus Teodorescu. Low-complexity online estimation for LiFePO4 battery state of charge in electric vehicles. *Journal of Power Sources*, 395:280–288, August 2018.

[14] Gregory L. Plett. Extended Kalman filtering for battery management systems of LiPB-based HEV battery packs: Part 2. Modeling and identification. *Journal of Power Sources*, 134(2):262–276, August 2004.

[15] C. M. Doyle. *Design and Simulation of Lithium Rechargeable Batteries*. PhD thesis, University of California, August 1995.

[16] Xinchen Zhao, Yilin Yin, Yang Hu, and Song-Yul Choe. Electrochemical-thermal modeling of lithium plating/stripping of Li(Ni0.6mn0.2co0.2)O2/Carbon lithium-ion batteries at subzero ambient temperatures. *Journal of Power Sources*, 418:61–73, April 2019.

[17] A. Bizeray, S. Duncan, and D. Howey. Advanced battery management systems using fast electrochemical modelling. In *IET Hybrid and Electric Vehicles Conference 2013 (HEVC 2013)*, pages 1–6, November 2013.

[18] Akram Eddahech, Olivier Briat, Mohamed Ayadi, and Jean-Michel Vinassa. Modeling and adaptive control for supercapacitor in automotive applications based on artificial neural networks. *Electric Power Systems Research*, 106:134–141, January 2014.

[19] Ephrem Chemali, Phillip J. Kollmeyer, Matthias Preindl, and Ali Emadi. State-of-charge estimation of Li-ion batteries using deep neural networks: A machine learning approach. *Journal of Power Sources*, 400:242–255, October 2018.

[20] Taimoor Zahid, Kun Xu, Weimin Li, Chenming Li, and Hongzhe Li. State of charge estimation for electric vehicle power battery using advanced machine learning algorithm under diversified drive cycles. *Energy*, 162:871–882, November 2018.

[21] Xiaoyu Li, Guodong Fan, Ke Pan, Guo Wei, Chunbo Zhu, Giorgio Rizzoni, and Marcello Canova. A physics-based fractional order model and state of energy estimation for lithium ion batteries. Part I: Model development and observability analysis. *Journal of Power Sources*, 367:187–201, November 2017.

[22] Jocelyn Sabatier, Junior Mbala Francisco, Franck Guillemard, Loic Lavigne, Mathieu Moze, and Mathieu Merveillaut. Lithium-ion batteries modeling: A simple fractional differentiation based model and its associated parameters estimation method. *Signal Processing*, 107:290–301, February 2015.

[23] Changfu Zou, Lei Zhang, Xiaosong Hu, Zhenpo Wang, Torsten Wik, and Michael Pecht. A review of fractional-order techniques applied to lithium-ion batteries, lead-acid batteries, and supercapacitors. *Journal of Power Sources*, 390:286–296, June 2018.

[24] Yunfeng Jiang, Bing Xia, Xin Zhao, Truong Nguyen, Chris Mi, and Raymond A. de Callafon. Data-based fractional differential models for non-linear dynamic modeling of a lithium-ion battery. *Energy*, 135:171–181, September 2017.

[25] Baojin Wang, Shengbo Eben Li, Huei Peng, and Zhiyuan Liu. Fractional-order modeling and parameter identification for lithium-ion batteries. *Journal of Power Sources*, 293:151–161, October 2015.

[26] Minghui Hu, Yunxiao Li, Shuxian Li, Chunyun Fu, Datong Qin, and Zonghua Li. Lithium-ion battery modeling and parameter identification based on fractional theory. *Energy*, 165:153–163, December 2018.

[27] Changfu Zou, Xiaosong Hu, Satadru Dey, Lei Zhang, and Xiaolin Tang. Nonlinear Fractional-Order Estimator with Guaranteed Robustness and Stability for Lithium-Ion Batteries. *IEEE Transactions on Industrial Electronics*, pages 1–1, 2017.

[28] Ivo Petráš. An Effective Numerical Method and Its Utilization to Solution of Fractional Models Used in Bioengineering Applications. *Advances in Difference Equations*, 2011(1):652789, March 2011.

[29] Jocelyn Sabatier, Om Prakash Agrawal, and J. A. Tenreiro Machado, editors. *Advances in Fractional Calculus*. Springer Netherlands, Dordrecht, 2007.

[30] Edmundo Capelas de Oliveira and José António Tenreiro Machado. A Review of Definitions for Fractional Derivatives and Integral. *Mathematical Problems in Engineering*, 2014:1–6, 2014.

[31] Manel Chetoui. *Identification de systèmes par modèle non entier à partir de signaux d'entrée sortie bruités*. PhD Thesis, 2013.

[32] B. M. Vinagre, I. Podlubny, and V. Feliu. Some approximations of fractional order operators used in control theory and applications. *Journal of Fractional Calculus and Applied Analysis*, pages 231–248, 2000.

[33] Stéphane Victor. *Identification par modèle non entier pour la poursuite robuste de trajectoire par platitude*. PhD Thesis, 2010.

[34] Denis Matignon. Stability properties for generalized fractional differential systems. In *Fractional Differential Systems: Models, Methods and Applications (FDS'98)*, volume 5, pages 145–158, Paris, FR, 1998.

[35] Lei Zhang, Xiaosong Hu, Zhenpo Wang, Fengchun Sun, and David G. Dorrell. Fractional-order modeling and State-of-Charge estimation for ultracapacitors. *Journal of Power Sources*, 314:28–34, May 2016.

[36] Hao Mu, Rui Xiong, Hongfei Zheng, Yuhua Chang, and Zeyu Chen. A novel fractional order model based state-of-charge estimation method for lithium-ion battery. *Applied Energy*, 207:384–393, December 2017.

[37] Uwe Westerhoff, Kerstin Kurbach, Frank Lienesch, and Michael Kurrat. Analysis of Lithium-Ion Battery Models Based on Electrochemical Impedance Spectroscopy. *Energy Technology*, 4(12):1620–1630, December 2016.

[38] Akram Eddahech, Olivier Briat, Nicolas Bertrand, Jean-Yves Delétage, and Jean-Michel Vinassa. Behavior and state-of-health monitoring of

Li-ion batteries using impedance spectroscopy and recurrent neural networks. *International Journal of Electrical Power & Energy Systems*, 42(1):487–494, November 2012.

[39] B. Wang, Z. Liu, S. E. Li, S. J. Moura, and H. Peng. State-of-Charge Estimation for Lithium-Ion Batteries Based on a Nonlinear Fractional Model. *IEEE Transactions on Control Systems Technology*, 25(1):3–11, January 2017.

[40] Yingzhi Cui, Pengjian Zuo, Chunyu Du, Yunzhi Gao, Jie Yang, Xinqun Cheng, Yulin Ma, and Geping Yin. State of health diagnosis model for lithium ion batteries based on real-time impedance and open circuit voltage parameters identification method. *Energy*, 144:647–656, February 2018.

[41] A. Oustaloup, P. Melchior, P. Lanusse, O. Cois, and F. Dancla. The CRONE toolbox for Matlab. In *CACSD. Conference Proceedings. IEEE International Symposium on Computer-Aided Control System Design (Cat. No.00TH8537)*, pages 190–195, Anchorage, AK, USA, 2000. IEEE.

[42] Aleksei Tepljakov. FOMCON: Fractional-Order Modeling and Control Toolbox. In *Fractional-order Modeling and Control of Dynamic Systems*, pages 107–129. Springer International Publishing, Cham, 2017.

[43] Tom T. Hartley and Carl F. Lorenzo. Fractional-order system identification based on continuous order-distributions. *Signal Processing*, 83(11):2287–2300, November 2003.

[44] Duarte Valério and José Sá da Costa. Finding a fractional model from frequency and time responses. *Communications in Nonlinear Science and Numerical Simulation*, 15(4):911–921, April 2010.

[45] C. Sanathanan and J. Koerner. Transfer function synthesis as a ratio of two complex polynomials. *IEEE Transactions on Automatic Control*, 8(1):56–58, January 1963.

[46] Ivo Petrás. Fractional Derivatives, Fractional Integrals, and Fractional Differential Equations in Matlab. In Ali H. Assi, editor, *Engineering Education and Research Using MATLAB*. IntechOpen, Rijeka, 2011.

[47] L. Dorcak. Numerical Models for the Simulation of the Fractional-Order Control Systems. *ArXiv Mathematics e-prints*, April 2002.

[48] Miassa Amira Taleb, Olivier Béthoux, and Emmanuel Godoy. Identification of a PEMFC fractional order model. *International Journal of Hydrogen Energy*, 42(2):1499–1509, January 2017.

[49] Abdelbaki Djouambi, Alina Voda Besancon, and Abdelfatah Charef. Fractional system identification using recursive algorithms approach. pages 1436–1441. IEEE, July 2007.

[50] Mohamed Aoun, Rachid Malti, Olivier Cois, and Alain Oustaloup. System identification using fractional hammerstein models. *IFAC Proceedings Volumes*, 35(1):265–269, 2002.

[51] Xiaoyu Li, Ke Pan, Guodong Fan, Rengui Lu, Chunbo Zhu, Giorgio Rizzoni, and Marcello Canova. A physics-based fractional order model and state of energy estimation for lithium ion batteries. Part II: Parameter identification and state of energy estimation for LiFePO 4 battery. *Journal of Power Sources*, 367:202–213, November 2017.

[52] Kodjo Senou Rodolphe Mawonou, Akram Eddahech, Didier Dumur, Emmanuel Godoy, Dominique Beauvois, and Michel Mensler. Li-ion battery pack soc estimation for electric vehicles. In *IECON 2018-44th Annual Conference of the IEEE Industrial Electronics Society*, pages 4968–4973. IEEE, 2018.